Crystallization Instead of Amorphization in Collision Cascades in Gallium Oxide

Junlei Zhao,[1,*] Javier García Fernández,[2] Alexander Azarov,[2] Ru He,[3] Øystein Prytz,[2] Kai Nordlund,[3] Mengyuan Hua,[1,†] Flyura Djurabekova,[3] and Andrej Kuznetsov[2,‡]

[1]*Department of Electronic and Electrical Engineering, Southern University of Science and Technology, Shenzhen 518055, China*

[2]*Department of Physics and Centre for Materials Science and Nanotechnology, University of Oslo, P.O. Box 1048 Blindern, N-0316 Oslo, Norway*

[3]*Department of Physics and Helsinki Institute of Physics, University of Helsinki, P.O. Box 43, Helsinki FI-00014, Finland*

(Received 7 March 2024; accepted 19 February 2025; published 25 March 2025)

Disordering of solids often leads to amorphization, but polymorph transitions, facilitated by favorable atomic rearrangements, may temporarily help to maintain long-range periodicity in the solid state. In far-from-equilibrium situations, such as atomic collision cascades, these rearrangements may not necessarily follow a thermodynamically gainful path, but may be kinetically limited. In this Letter, we focus on such crystallization instead of amorphization in collision cascades in gallium oxide (Ga_2O_3). We determine the disorder threshold for irreversible $\beta \rightarrow \gamma$ polymorph transition and explained why it results in elevating energy to that of the γ polymorph, which exhibits the highest polymorph energy in the system below the amorphous state. Specifically, we demonstrate that upon reaching the disorder transition threshold, the Ga sublattice kinetically favors transitioning to the γ-like configuration, requiring significantly less migration for Ga atoms to reach the lattice sites during postcascade processes. As such, our data provide a consistent explanation of this remarkable phenomenon and can serve as a toolbox for predictive multipolymorph fabrication.

DOI: 10.1103/PhysRevLett.134.126101

Although amorphization in cascades is common in many materials, a few reports in literature confirm radiation-induced polymorph transitions [1,2]. Nevertheless, until recently, interest in such crystallization instead of amorphization phenomenon was primarily maintained within the specialized radiation effect research community, despite great options for tuning functional properties, however in reality limited by challenges to demonstrate the well-defined structures commonly required in technology. This was the status quo until Azarov *et al.* [3] demonstrated a regularly shaped new polymorph thin film on the top of the initial polymorph substrate, as a result of the radiation-induced disordering in gallium oxide (Ga_2O_3). This work attracted significant attention of a broader research community, inspired by this novel opportunity to design new functionalities out of Ga_2O_3 polymorph stacks, potentially useful in a range of Ga_2O_3 technologies from power electronics [4,5] to solar-blind ultraviolet optoelectronics [6,7]. In the majority of Ga_2O_3 polymorph transition studies thus far, monoclinic $\beta - Ga_2O_3$ (12, $C2/m$) was used as the initial material, being selected as the thermodynamically stable form of Ga_2O_3. Additionally, four metastable Ga_2O_3 polymorphs (sorted as $\beta < \kappa < \alpha < \delta < \gamma$ with respect to the ascending order of the zero-strain potential energies) have been reported in the literature [8–13]. The amorphous Ga_2O_3 phase was proven to be synthesized via several methods [14,15], whereas its amorphization under irradiation is suppressed by phase transitions in cascades.

Initial reports [2,3] identified the disorder-induced polymorph as the orthorhombic κ-Ga_2O_3 (33, $Pna2_1$) accounting for its second lowest energy also supported by the electron microscopy identification but at that time performed along one zone-axis only. Later works [16–20] unambiguously identified the newly formed polymorph as cubic defective spinel γ-Ga_2O_3 (227, $Fd\bar{3}m$) based on multiple zone-axis microscopy investigations. Thus, although there is a consensus in the literature that the disorder-induced $\beta \rightarrow \gamma$ phase transition in Ga_2O_3 occurs instead of amorphization, no clear explanation exists for why the transition lifts the system energy to that of the highest among Ga_2O_3 polymorphs, suggesting a kinetically limited process. Moreover, despite the considerable data already collected on radiation-induced polymorphism in Ga_2O_3, the disorder thresholds enabling the transition remain imprecisely determined, hindering predictive modeling for potential applications. Here, we show that the $\beta \rightarrow \gamma$ phase transition occurs remarkably swiftly, governed by a sharp disorder threshold. By leveraging machine-learning molecular dynamics [21], we pinpoint this narrow threshold range of disorder that triggers the irreversible $\beta \rightarrow \gamma$ phase transition during postcascade evolution.

*Contact author: zhaojl@sustech.edu.cn

†Contact author: huamy@sustech.edu.cn

‡Contact author: andrej.kuznetsov@fys.uio.no

 © 2025 American Physical Society

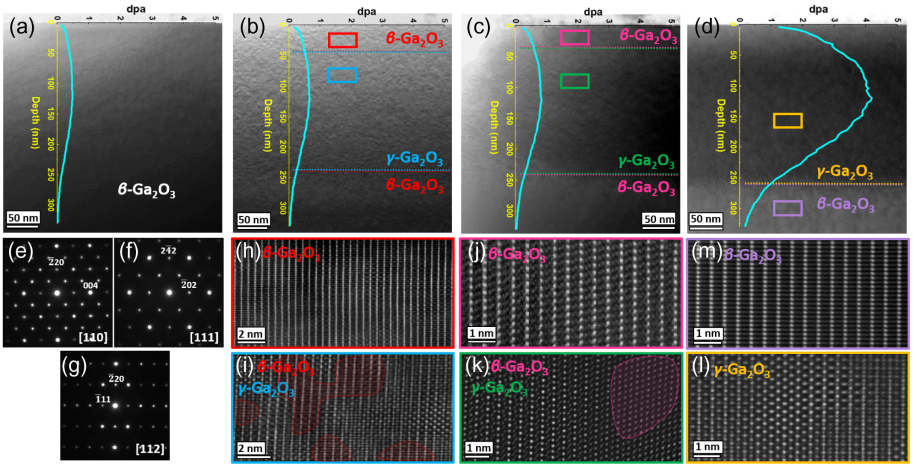

FIG. 1. Swift $\beta \rightarrow \gamma Ga_2O_3$ phase transition controlled by a disorder threshold. Bright-field STEM images showing fully implanted regions of the β samples irradiated with (a) 1.2×10^{14}, (b) 1.6×10^{14}, (c) 2.0×10^{14}, and (d) 1.0×10^{15} 400 keV $^{58}Ni^{+}cm^{-2}$, corresponding to 0.50, 0.65, 0.85, and 4.15 displacements per atom (dpa) at the depth of the maximum disorder. The cyan curves show the corresponding damage levels in dpa unit, derived from SRIM simulations. The dashed lines in (b)–(d) mark the positions of the established top β/γ and bottom γ/β interfaces The colored boxes highlight the exact positions of the corresponding atomic-resolution STEM images in (h)–(l). (e)–(g) The SAED patterns of the γ phase collected along the [110], [111], [112] zone axes, respectively. (h)–(l) Atomic-resolution STEM images obtained from the samples in (b)–(d), linked by the box colors. (h),(j),(m) Focus on the β regions, while (i), (k), and (l) focus on the γ regions.

Figure 1 summarizes scanning transmission electron microscopy (STEM) data used to monitor the onset of the disorder-induced $\beta \rightarrow \gamma$ phase transition and to determine the required disorder threshold for this transition [Supplemental Material (SM) [22], Appendix I for experimental details]. Specifically, Figs. 1(a)–1(d) show STEM images of samples implanted with four different fluences of 400 keV $^{58}Ni^{+}$ ions. Figures 1(e)–1(g) show selected-area electron diffraction (SAED) patterns of the γ phase collected along the three different zone axes. Concurrently, Figs. 1(h)–1(l) show atomic-resolution images recorded from different parts of the samples in accordance with the frame color codes. Visually different orientations and scales of the Ga planes in Figs. 1(h), 1(j), and 1(m) attribute sorely to variations in observation angles and magnifications, otherwise verifying the same atomistic structure of the β phase. Atomic-resolution images in Figs. 1(i), 1(k), and 1(l) are taken from inside the disordered layer of the samples in Figs. 1(b)–1(d), respectively, clearly resolving γ-Ga planes.

Figure 1 provides clear evidence that the $\beta \rightarrow \gamma$ phase transition is a function of disorder, consistent with the dpa depth profiles. A careful inspection of the sample in Fig. 1(a), exposed to 0.50 dpa in maximum, reveals only the β-phase features throughout the irradiated sample. In contrast, with a slight increase in fluence, reaching 0.65 dpa in maximum, we detect the onset of the $\beta \rightarrow \gamma$ phase transition, featured by the formation of the β-γ mixed layer [Fig. 1(i)] sandwiched between the remaining β film [Fig. 1(b)]. The β-γ mixed layer consists of approximately 50–50 proportion [Fig. 1(i)]. Increasing disorder toward 0.85 dpa in maximum leads to the broadening of the mixed layer [Fig. 1(c)] and an increase of the γ-phase fraction in this layer to $\leq 90\%$ [Fig. 1(k)]. A further increase in dpa results in the formation of the homogeneous γ layer on top of the β-phase substrate [Figs. 1(d), 1(m), and 1(l)], consistent with the literature [16,18]. Additionally, local stoichiometry is preserved with the maximum incorporated Ni concentration of $\sim 5 \times 10^{19}$ cm^{-3} for the highest ion dose [18].

Therefore, a 0.65–0.85 dpa level is sufficient to first overcome the nucleation barrier and then stabilize the γ phase at the specific temperature and dose rate used in this experiment (under conditions of the survival rate of primary damage interconnected with dpa; see Ref. [50]). The importance of postcascade defect reactions becomes apparent when comparing the dpa values at the top β/γ and bottom γ/β interfaces for the samples in Figs. 1(b) and 1(c). A higher dpa value at the top β/γ interface indicates that the disorder required for the phase transition depends on the proximity of the sample surface that acts as a sink for the radiation-induced defects, correlating between the advancements of the top β/γ and bottom γ/β interfaces and the dpa values. In the sample with the highest fluence [Fig. 1(d)], the dpa value at the bottom γ/β interface is significantly higher than that at the same γ/β interfaces in the samples irradiated with lower fluences [Figs. 1(b) and 1(c)], confirming a nonlinearity in the defect survival rate as a function of cascade density [51]. Nevertheless, the overall trend is clear: the nucleation of the γ phase starts upon reaching a disorder threshold in the maximum of the nuclear energy deposition region, corresponding to the depth where the dpa value is maximal, leading to its

expansion toward the surface and into the bulk with increasing fluence.

In Fig. 2, machine-learning molecular dynamics simulations reveal the atomic-level mechanism of the swift $\beta \rightarrow \gamma$ phase transition in the experimental dpa range. Commencing with the pristine β-Ga_2O_3 lattice (see SM, Appendix II, for computational details), stochastic overlapping cascades initially generate primary damage as discrete point defect clusters [Fig. 2(a)]. These defect clusters subsequently merge into a continuous disordered matrix [Fig. 2(b)]. This evolution is clearly traceable through changes in the β-lattice pattern viewed from the β[010] orientation, which gradually disappears with the increasing number of primary knock-on atoms (PKAs). A distinct difference is observed between the $\beta + 400$-PKA and $\beta + 600$-PKA cells [Figs. 2(a) and 2(b)] when the accumulated disorder completely fills the cell.

Evolution of potential energy, ΔE_p, is compared across two independent simulations starting with β- and γ-Ga_2O_3 cells [Fig. 2(c)] (SM, Appendixes III and IV, Figs. S3 and S4). Initially, the ΔE_p of γ phase is ~0.031 eV/atom higher than that of the β phase. The fast increasing trend in the β-phase curve during the early stages of the overlapping cascades (0–200 PKAs) signifies discrete primary damage accumulation. However, this trend slows down as newly generated defect clusters merge with the previously generated ones, leading to damage saturation. A similar trend is observed in the γ-phase curve, albeit with a significantly smaller gradient comparing to that for β phase. This is consistent with the high radiation tolerance of the defective spinel structure of the γ phase, which is insensitive to the formation of new point defects in collision cascades [18]. The two curves intersect after 350 PKAs, prominently correlating with the similarity analysis of the partial radial distribution functions (PRDFs) (SM, Appendix IV, Fig. S5). After the crossing point, the β-phase ΔE_p is higher than the γ-phase one, indicating that the consequent cascades disorder the β phase more intensively than the γ phase. At the highest disorder level (800 PKAs), both cells still exhibit significant energy differences (0.03–0.04 eV/atom) comparing to that of the amorphous Ga_2O_3 [marked as green zone in Fig. 2(c)]. Thus, for both phases, this disordering effect does not cause transition to amorphization, otherwise commonly observed in semiconductors under ion-beam irradiation [52,53]. The analyses of the PRDFs and bond-angle distributions confirm that the β-O sublattice retains its face-centered cubic lattice after 800 PKAs (SM, Appendix IV, Figs. S5 and S6).

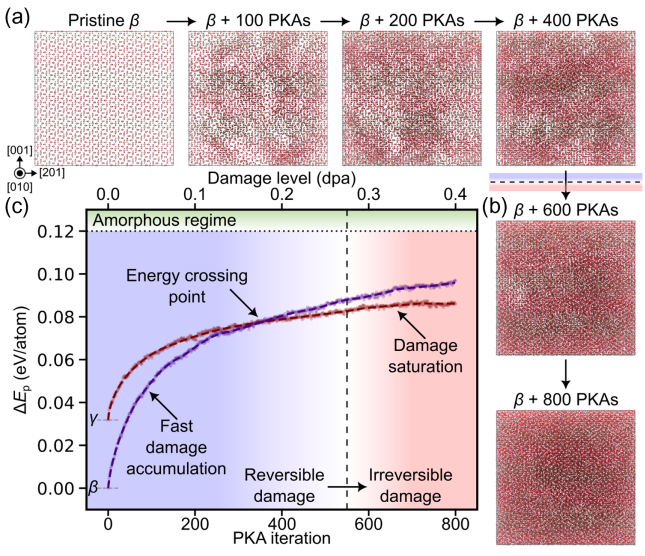

FIG. 2. Structural evolution of β-Ga_2O_3 exposed to overlapping cascades classified as (a) below the reversible damage threshold, and (b) above the irreversible transition damage threshold. The O and Ga atoms are in red and brown, respectively. (c) ΔE_p versus PKAs relative to the perfect β phase's potential energy as a zero point. The dashed line is drawn at 550 PKAs, discussed later in Fig. 3. See SM, Appendix VI, for the shared data of the detailed molecular dynamics cells [22].

Furthermore, we investigate the structural evolution in the β-phase cells due to the recovery of the damage accumulated at different dpa levels. Annealing simulations at 1500 K and 0 bar are summarized in Fig. 3. Figure 3(a) illustrates seven distinct configurations after the annealing, as viewed from β[001] orientation. In Fig. 3(b), we display the corresponding final ΔE_p with respect to a zero-point corresponding to the pristine β phase, and the brown line indicating the pristine γ phase under the same annealing conditions (SM, Appendix IV, Fig. S9). The PRDFs of the second Ga-Ga shell are used for a similarity analysis. In Fig. 3(c), the Pearson correlation coefficients (Pr) are calculated with respect to the pristine β-Ga (purple line) and γ-Ga (brown lines) PRDFs as a function of PKAs.

Combining the analyses of the lattice configurations, the final ΔE_p, and Pr data, the postannealing states exhibit a sharp change starting in the range of 450–500 PKAs. Consequently, in accordance with the analysis in Fig. 2, the initial damage level of 0.25–0.3 dpa is interpreted as the critical disorder threshold. Thus, the simulated dpa level required for the irreversible $\beta \rightarrow \gamma$ transition aligns remarkably well with the experimental and SRIM data in Fig. 1. The mechanism of the irradiation-induced $\beta \rightarrow \gamma$ transition is illustrated in Fig. 3(d). The irradiation-induced disorder primarily introduces Ga defect clusters that reorder during postcascade periods. At low-dpa levels, these Ga defect clusters are sparsely embedded in the β phase and can swiftly recover due to the rapid migration of Ga atoms [54–58] and the recombination of Frenkel pairs [59]. Conversely, the critical damage level is reached when the accumulated Ga defect clusters completely replace the original β phase. The system with high potential energy becomes rather unstable and can only exist transiently. Instead of reverting to the monoclinic β lattice, the Ga sublattice kinetically favors transitioning to the metastable cubic γ lattice, requiring significantly less migration of Ga atoms to reach the lattice sites.

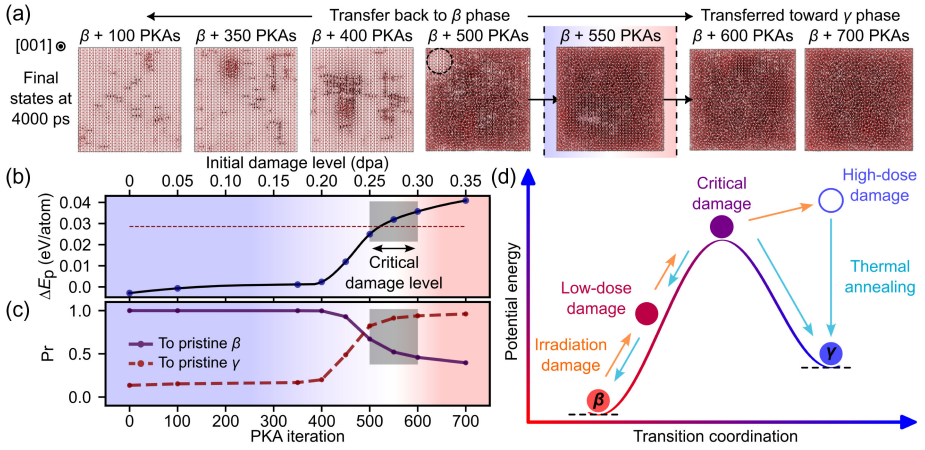

FIG. 3. (a) Postannealing states starting from different β+ PKA states. The $\beta + 500$ PKA cell results in recovery of a fraction of the β phase (dashed circle). (b) Final ΔE_p and (c) Pr values versus PKAs. The irreversible transition damage threshold is pinpointed at 550 PKAs, ~0.275 dpa. See SM, Appendix IV, Figs. S7–S9 for additional analyses. (d) Schematics of the $\beta \rightarrow \gamma$ phase transition mechanism in collision cascades.

Figures 1–3 elucidate the $\beta \rightarrow \gamma$ phase transition in stochastic dynamical systems. However, it is instructive to isolate two otherwise coupled processes, internal atom migration and external stress release, to present the kinetically minimized atomic migration pathways in the Ga sublattice. An 80-atom orthogonal supercell is used as the smallest cell to illustrate the overall symmetry transition of the initial monoclinic β-Ga [Fig. 4(a)]. Short-range migrations involving precisely half of the total Ga atoms (16 out of 32) complete the internal atomic transition. These Ga atoms are highlighted in Fig. 4(a) and indexed based on the migration sequences in Fig. 4(d), resulting in a minimal effective dpa of 0.20 (16 displaced atoms out of 80), aligning excellently with the critical dpa level (0.25–0.30) in Fig. 3(d). In total, 12 tetrahedral Ga (Ga_T) and four octahedral Ga (Ga_O) atom displacements yield eight new Ga_T and eight Ga_O. The Ga_T-Ga_O ratio changes from 1:1 to 3:5, with four unoccupied Ga_O sites completing a defect-free spinel Ga_3O_4 lattice. The intermediate γ' phase [Fig. 4(b)] displays the typical hexagonal projected pattern of the γ-Ga sublattice viewed from the $\gamma[011]$ and $\gamma[0\bar{1}1]$ directions (SM, Appendix V, Fig. S10, and Video S1). Nevertheless, the γ' phase retains the β-phase cell side length, leading to a nonuniform external stress (and strain) accumulating in the system. Thus, the phase transition is further finalized via cell relaxation, associated with marginal internal atom rearrangement at local sites [Fig. 4(c)]. This scenario is supported by the experimental observation of the strain release accompanying with the $\beta \rightarrow \gamma$ phase transition measured by SAED [3,16,18].

In a real material system, internal atom migration and external stress release are naturally combined during phase transition. Therefore, the energy evolution of the fixed (F) and unfixed (U) cells is calculated using density functional theory and the two machine-learning interatomic potentials (SM, Appendix II) to map the potential energy landscape [Fig. 4(d)]. The overall trends predicted by all three models are comparable, with the highest energy increase reaching

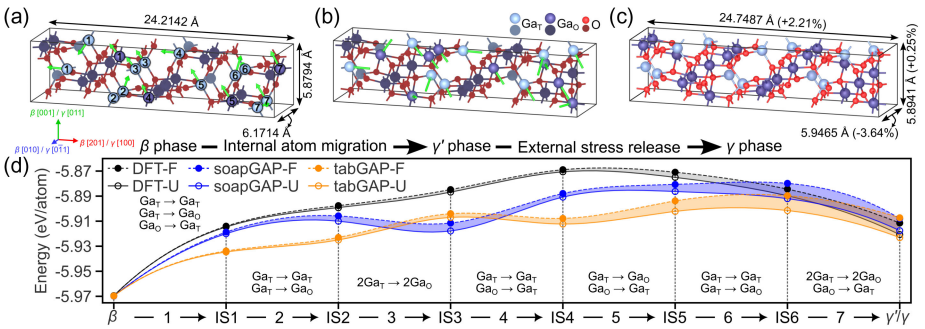

FIG. 4. (a) An initial β-phase supercell with Ga_T, Ga_O, and O colored in light blue, dark blue, and red, respectively. The 16 migrating Ga atoms are highlighted with the indices of migration sequence from 1 to 7, corresponding to the indices in (d). The green arrows are the displacement vectors. (b) The γ' phase after Ga atom migration. (c) The final γ phase after external stress release. (d) The potential energy landscape of the pathways, probed using density-functional theory, soapGAP, and tabGAP, from β to γ'/γ phases with six intermediate states (IS1–IS6). The systems are optimized with both fixed (F) and unfixed (U) cell side lengths.

~0.12 eV/atom above the energy of the β phase. The overall transition pathways can be divided into seven migration sequences with six intermediate states [IS1–IS6 in Fig. 4(d)]. Each migration sequence involves two or three Ga atom displacements, and significant stress release is only observed after a majority of the Ga have been displaced [from IS4 to γ'/γ in Fig. 4(d)]. The fact that the disorder threshold required for $\beta \rightarrow \gamma$ phase transition is consistently close to 0.2 dpa is not a coincidence, but is a natural consequence of the transition pathways allowing the minimal kinetics with the lowest disorder threshold. While comparing with experiment, the defect recombination and repetitive atom displacement can be the factors requiring disorders larger than 0.2 dpa for making the $\beta \rightarrow \gamma$ phase transition sustainable.

In this Letter, we show that amorphization is suppressed by the polymorphic $\beta \rightarrow \gamma$ phase transition. We accurately determine the critical disorder level that triggers the transition from disorder state to γ phase. Below this threshold, the high-energy γ-Ga_2O_3 forms only transiently. However, upon reaching the threshold, instead of reverting to the β phase, the Ga sublattice kinetically favors transitioning to the γ phase, requiring significantly less migration for Ga atoms to reach the γ-lattice sites during the postcascade processes. Moreover, we describe full atomic-level migration pathways of $\beta \rightarrow \gamma$ phase transition involving only short-distance β-Ga displacements together with external stress release. Notably, this approach can be generalized and used for studying lattice phase transitions of other oxide systems.

Acknowledgments—This work was supported by National Natural Science Foundation of China under Grants 62304097 and 62374079; Guangdong Basic and Applied Basic Research Foundation under Grant 2023A1515012048; Shenzhen Fundamental Research Program under Grants JCYJ20230807093609019, JCYJ20240807170626004, JCYJ20220530114615035, and 2023112115707001. M-ERA.NET Program is acknowledged for financial support via GOFIB project (administrated by the Research Council of Norway Project No. 337627 in Norway and the Academy of Finland Project No. 352518 in Finland). The experimental infrastructures were provided at the Norwegian Micro- and Nano-Fabrication Facility, NorFab, supported by the Research Council of Norway Project No. 295864, at the Norwegian Centre for Transmission Electron Microscopy, NORTEM, supported by the Research Council of Norway Project No. 197405. The researchers mobility was partly supported by the INTPART program at the Research Council of Norway via Project No. 322382. The computational resource is supported by the Center for Computational Science and Engineering at the Southern University of Science and Technology. The authors are also grateful to the grants of computer power from CSC-IT Center for Science, Finland.

Data availability—The data that support the findings of this Letter are openly available at [60].

[1] G. R. Lumpkin, K. L. Smith, M. G. Blackford, B. S. Thomas, K. R. Whittle, N. A. Marks, and N. J. Zaluzec, Phys. Rev. B **77**, 214201 (2008).
[2] E. A. Anber, D. Foley, A. C. Lang, J. Nathaniel, J. L. Hart, M. J. Tadjer, K. D. Hobart, S. Pearton, and M. L. Taheri, Appl. Phys. Lett. **117**, 152101 (2020).
[3] A. Azarov, C. Bazioti, V. Venkatachalapathy, P. Vajeeston, E. Monakhov, and A. Kuznetsov, Phys. Rev. Lett. **128**, 015704 (2022).
[4] A. J. Green *et al.*, APL Mater. **10**, 029201 (2022).
[5] M. J. Tadjer, Science **378**, 724 (2022).
[6] A. S. Pratiyush, S. Krishnamoorthy, R. Muralidharan, S. Rajan, and D. N. Nath, 16-advances in Ga_2O_3 solar-blind UV photodetectors, in *Gallium Oxide*, Metal Oxides, edited by S. Pearton, F. Ren, and M. Mastro (Elsevier, Amsterdam, The Netherlands, 2019), pp. 369–399.
[7] S. Kim and J. Kim, Appl. Phys. Lett. **117**, 261101 (2020).
[8] R. Roy, V. G. Hill, and E. F. Osborn, J. Am. Chem. Soc. **74**, 719 (1952).
[9] S. Yoshioka, H. Hayashi, A. Kuwabara, F. Oba, K. Matsunaga, and I. Tanaka, J. Phys. Condens. Matter **19**, 346211 (2007).
[10] J. E. N. Swallow *et al.*, Chem. Mater. **32**, 8460 (2020).
[11] S. Mu and C. G. Van de Walle, Phys. Rev. Mater. **6**, 104601 (2022).
[12] L. E. Ratcliff *et al.*, Adv. Mater. **34**, 2204217 (2022).
[13] T. Kato, H. Nishinaka, K. Shimazoe, K. Kanegae, and M. Yoshimoto, ACS Appl. Electron. Mater. **5**, 1715 (2023).
[14] K. R. Gann, C. S. Chang, M.-C. Chang, D. R. Sutherland, A. B. Connolly, D. A. Muller, R. B. van Dover, and M. O. Thompson, Appl. Phys. Lett. **121**, 062102 (2022).
[15] Y. Liu, H. Liang, L. Yang, G. Yang, H. Yang, S. Song, Z. Mei, G. Csányi, and B. Cao, Adv. Mater. **35**, 2210873 (2023).
[16] J. García-Fernández, S. B. Kjeldby, P. D. Nguyen, O. B. Karlsen, L. Vines, and Ø. Prytz, Appl. Phys. Lett. **121**, 191601 (2022).
[17] T. Yoo, X. Xia, F. Ren, A. Jacobs, M. J. Tadjer, S. Pearton, and H. Kim, Appl. Phys. Lett. **121**, 072111 (2022).
[18] A. Azarov, J. G. Fernández, J. Zhao, F. Djurabekova, H. He, R. He, Ø. Prytz, L. Vines, U. Bektas, P. Chekhonin, N. Klingner, G. Hlawacek, and A. Kuznetsov, Nat. Commun. **14**, 4855 (2023).
[19] H.-L. Huang, C. Chae, J. M. Johnson, A. Senckowski, S. Sharma, U. Singisetti, M. H. Wong, and J. Hwang, APL Mater. **11**, 061113 (2023).
[20] H.-L. Huang, J. M. Johnson, C. Chae, A. Senckowski, M. H. Wong, and J. Hwang, Appl. Phys. Lett. **122**, 251602 (2023).
[21] J. Zhao, J. Byggmästar, H. He, K. Nordlund, F. Djurabekova, and M. Hua, npj Comput. Mater. **9**, 159 (2023).
[22] See Supplemental Material at http://link.aps.org/supplemental/10.1103/PhysRevLett.134.126101, which includes Refs. [23–49], for additional information about the experimental and computational methods and detailed analyses.

[23] A. I. Titov, A. Y. Azarov, L. M. Nikulina, and S. O. Kucheyev, Nucl. Instrum. Methods Phys. Res., Sect. B **256**, 207 (2007).
[24] J. F. Ziegler, M. D. Ziegler, and J. P. Biersack, Nucl. Instrum. Methods Phys. Res., Sect. B **268**, 1818 (2010).
[25] W. J. Weber and Y. Zhang, Curr. Opin. Solid State Mater. Sci. **23**, 100757 (2019).
[26] S. Agarwal, Y. Lin, C. Li, R. E. Stoller, and S. J. Zinkle, Nucl. Instrum. Methods Phys. Res., Sect. B **503**, 11 (2021).
[27] Y.-R. Lin, S. J. Zinkle, C. J. Ortiz, J.-P. Crocombette, R. Webb, and R. E. Stoller, Curr. Opin. Solid State Mater. Sci. **27**, 101120 (2023).
[28] B. R. Tuttle, N. J. Karom, A. O'Hara, R. D. Schrimpf, and S. T. Pantelides, J. Appl. Phys. **133**, 015703 (2023).
[29] S. Plimpton, J. Comp. Physiol. **117**, 1 (1995).
[30] A. P. Bartók, M. C. Payne, R. Kondor, and G. Csányi, Phys. Rev. Lett. **104**, 136403 (2010).
[31] A. P. Bartók, R. Kondor, and G. Csányi, Phys. Rev. B **87**, 184115 (2013).
[32] M. W. Finnis and J. E. Sinclair, Philos. Mag. A **50**, 45 (1984).
[33] J. Byggmästar, K. Nordlund, and F. Djurabekova, Phys. Rev. Mater. **6**, 083801 (2022).
[34] Supplementary data: complex Ga_2O_3 polymorphs explored by accurate and general-purpose machine-learning interatomic potentials, 10.6084/m9.figshare.21731426 (2022).
[35] K. Nordlund, Comput. Mater. Sci. **3**, 448 (1995).
[36] K. Nordlund, M. Ghaly, R. S. Averback, M. Caturla, T. Diaz de la Rubia, and J. Tarus, Phys. Rev. B **57**, 7556 (1998).
[37] B. Dünweg and W. Paul, Int. J. Mod. Phys. C **02**, 817 (1991).
[38] G. Kresse and J. Furthmüller, Comput. Mater. Sci. **6**, 15 (1996).
[39] P. E. Blöchl, Phys. Rev. B **50**, 17953 (1994).
[40] J. P. Perdew, K. Burke, and M. Ernzerhof, Phys. Rev. Lett. **77**, 3865 (1996).
[41] A. H. Larsen *et al.*, J. Phys. Condens. Matter **29**, 273002 (2017).
[42] K. Momma and F. Izumi, J. Appl. Crystallogr. **44**, 1272 (2011).
[43] A. Stukowski, Model. Simul. Mater. Sci. Eng. **18**, 015012 (2010).
[44] J. Åhman, G. Svensson, and J. Albertsson, Acta Crystallogr. Sect. C **52**, 1336 (1996).
[45] H. Y. Playford, A. C. Hannon, E. R. Barney, and R. I. Walton, Chem.-Eur. J. **19**, 2803 (2013).
[46] H. Y. Playford, A. C. Hannon, M. G. Tucker, D. M. Dawson, S. E. Ashbrook, R. J. Kastiban, J. Sloan, and R. I. Walton, J. Phys. Chem. C **118**, 16188 (2014).
[47] γ-Ga_2O_3 ($Ga_{2.67}O_4$ m) crystal structure.
[48] I. Cora, Z. Fogarassy, R. Fornari, M. Bosi, A. Rečnik, and B. Pécz, Acta Mater. **183**, 216 (2020).
[49] J. L. Yarnell, M. J. Katz, R. G. Wenzel, and S. H. Koenig, Phys. Rev. A **7**, 2130 (1973).
[50] A. Azarov, C. Radu, A. Galeckas, I. F. Mercioniu, A. Cernescu, V. Venkatachalapathy, E. Monakhov, F. Djurabekova, C. Ghica, J. Zhao, and A. Kuznetsov, Nano Lett. **25**, 1637 (2025).
[51] A. Azarov, V. Venkatachalapathy, P. Karaseov, A. Titov, K. Karabeshkin, A. Struchkov, and A. Kuznetsov, Sci. Rep. **12**, 15366 (2022).
[52] J. Nord, K. Nordlund, and J. Keinonen, Phys. Rev. B **65**, 165329 (2002).
[53] L. Pelaz, L. A. Marqués, and J. Barbolla, J. Appl. Phys. **96**, 5947 (2004).
[54] M. A. Blanco, M. B. Sahariah, H. Jiang, A. Costales, and R. Pandey, Phys. Rev. B **72**, 184103 (2005).
[55] A. Kyrtsos, M. Matsubara, and E. Bellotti, Phys. Rev. B **95**, 245202 (2017).
[56] Y. K. Frodason, C. Zimmermann, E. F. Verhoeven, P. M. Weiser, L. Vines, and J. B. Varley, Phys. Rev. Mater. **5**, 025402 (2021).
[57] A. Azarov, V. Venkatachalapathy, E. V. Monakhov, and A. Y. Kuznetsov, Appl. Phys. Lett. **118**, 232101 (2021).
[58] Y. K. Frodason, J. B. Varley, Klaus Magnus H. Johansen, L. Vines, and C. G. Van de Walle, Phys. Rev. B **107**, 024109 (2023).
[59] H. He, J. Zhao, J. Byggmästar, R. He, K. Nordlund, C. He, and F. Djurabekova, Acta Mater. **276**, 120087 (2024).
[60] Supplemental data: crystallization instead of amorphization in collision cascades in gallium oxide, 10.6084/m9.figshare.26183537 (2024).